



LAWRENCE  
LIVERMORE  
NATIONAL  
LABORATORY

# Effect of the mounting membrane on shape in ICF implosions

S. R. Nagel, S. W. Haan, J. R. Rygg, M. Barrios, L. R. Benedetti, D. K. Bradley, J. E. Field, B. A. Hammel, N. Izumi, O. S. Jones, S. F. Khan, T. Ma, A. E. Pak, R. Tommasini, R. P. J. Town

November 25, 2014

Physics of Plasmas

## **Disclaimer**

---

This document was prepared as an account of work sponsored by an agency of the United States government. Neither the United States government nor Lawrence Livermore National Security, LLC, nor any of their employees makes any warranty, expressed or implied, or assumes any legal liability or responsibility for the accuracy, completeness, or usefulness of any information, apparatus, product, or process disclosed, or represents that its use would not infringe privately owned rights. Reference herein to any specific commercial product, process, or service by trade name, trademark, manufacturer, or otherwise does not necessarily constitute or imply its endorsement, recommendation, or favoring by the United States government or Lawrence Livermore National Security, LLC. The views and opinions of authors expressed herein do not necessarily state or reflect those of the United States government or Lawrence Livermore National Security, LLC, and shall not be used for advertising or product endorsement purposes.

# Effect of the mounting membrane on shape in ICF implosions

S. R. Nagel,\* S. W. Haan, J. R. Rygg, M. Barrios, L. R. Benedetti, D. K. Bradley, J. E. Field, B. A. Hammel, N. Izumi, O. S. Jones, S. F. Khan, T. Ma, A. E. Pak, R. Tommasini, and R. P. J. Town  
*Lawrence Livermore National Laboratory, P.O. Box 808, Livermore, California 94551-0808, USA*  
(Dated: January 6, 2015)

The performance of Inertial Confinement Fusion (ICF) targets relies on the symmetric implosion of highly compressed fuel. X-ray area-backlit imaging is used to assess in-flight low mode 2D asymmetries of the shell. These time-resolved images of the shell exhibit features that can be related to the lift-off position of the membranes used to hold the capsule within the hohlraum. Here we describe a systematic study of this membrane or “tent” thickness and its impact on the measured low modes for in-flight and self-emission images. The low mode amplitudes of the shell in-flight shape ( $P_2$  and  $P_4$ ) are weakly affected by the tent feature in time-resolved, backlit data. By contrast, time integrated self-emission images along the same axis exhibit a reversal in perceived  $P_4$  mode due to growth of a feature seeded by the tent, which can explain prior inconsistencies between the in-flight  $P_4$  and core  $P_4$ , leading to a reevaluation of optimum hohlraum length. Simulations with a tent-like feature normalized to match the feature seen in the backlit images predict a very large impact on the capsule performance from the tent feature.

## I. INTRODUCTION

At the National Ignition Facility (NIF)[1] scientists are investigating the indirect drive approach to ICF [2, 3], in which a layered DT-filled capsule is placed inside a high-Z hohlraum, with the goal to achieve fusion ignition and burn. To form a central hot spot with sufficient temperature and areal density to achieve ignition and high gain in ICF requires highly symmetric implosion of the capsule. The hot spot self-emission can be misleading as to the symmetry of the stagnated shell [4]. Therefore the shape of the implosion is diagnosed by both time resolved x-ray radiography of the capsule [5] and imaging of the x-ray hot spot self-emission [6].

In ICF the growth of the Rayleigh-Taylor Instability (RTI) [7–9] is of concern. It occurs at the interface of two fluids with different densities when the interface is accelerated into the denser fluid. RTI can be seeded by perturbations on the capsule, which can lead to small perturbations growing exponentially and can be detrimental to ICF at two stages [3]. RTI can lead to rupturing of the shell during ablation. In the second stage, which occurs when the shell is slowed down by the pressure from the hot spot, RTI can lead to mixing of the dense cold fuel layer with the hot spot, reducing the effective size and deforming the shape of the hot spot.

To quantify the shape of the imploding capsule, images of the imploding shell and of the hot spot are taken, using backlit x-ray radiography and self emission respectively. The radiography results in a projection of the spherical harmonics  $Y_{lm}$  onto a 2D image. The effects discussed here are azimuthally-symmetric and the analysis uses  $Y_{l0}$  which are the Legendre polynomials  $P_l$ . Here  $l=0-8$  are considered low mode.

It has been found that the membrane mounting the

capsule within the hohlraum interferes with the interpretation of the low mode shape for the low-foot (low adiabat) laser drive. By varying only the membrane thickness, we have isolated the influence of the membrane on the shape of the x-ray emission on a low convergence platform. Here we correlate the measurements to simulations and discuss the expected impact of the membrane on the performance of high convergence ICF experiments.

## II. EXPERIMENTAL SETUP

The indirect drive target consists of a NIF ignition scale (diameter of 5750  $\mu\text{m}$  and length of 9425  $\mu\text{m}$ ) [10, 11] hohlraum target modified for backlit imaging [5, 12, 13]. The backlit imaging technique has been developed [5] to radiograph the imploding capsule in-flight from a radius of approximately 300  $\mu\text{m}$  to about 150  $\mu\text{m}$ . Probing to even smaller radii is currently being investigated. In this technique two of the NIFs 48 quads are redirected from the hohlraum to a germanium foil located 12 mm from the capsule center in the equatorial plane. This generates 10.25 keV Ge He $_{\alpha}$  x-rays over a  $\sim 1$  mm diameter spot lasting about 2 ns. To provide a line-of-sight from the Ge backlighter foil through the hohlraum to the gated x-ray detector, two  $0.9 \times 0.83$  mm diagnostic holes are cut out of opposite sides of the hohlraum wall and plugged by high-density carbon (HDC) windows.

The length of the cylindrical gold hohlraum was varied between  $-300$  to  $+1000$   $\mu\text{m}$  from the original design length of 9.4 mm. The capsule, with a 1.15 mm outer radius and 0.21 mm thick spherical plastic shell, is filled with 6.7 mg/cm $^3$  of 30% of D $_2$  and 70% of  $^3\text{He}$  gas when cooled to 24 K. The hohlraum is driven with a 1.3 MJ, 21 ns long, shaped ignition pulse as described in [5].

The capsule is held at the center of the hohlraum by two thin plastic membranes that are called tents. On early NIF shots, the tent membrane was 300 nm thick; as technology improved, targets were built with 110 nm,

---

\*Electronic address: nagel7@llnl.gov

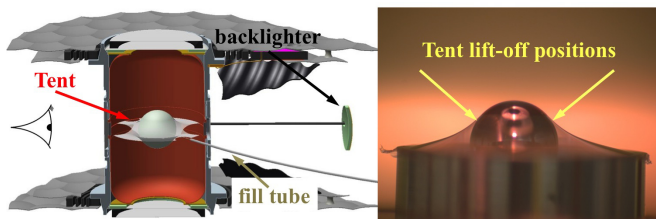


FIG. 1: (Color) Illustration of the tent mounted capsule within the hohlraum in a backlit platform target and an image of the tent lifting off the capsule.

45 nm, 30 nm, and most recently as thin as 12 nm tents. It should be noted that as the tent becomes thinner it becomes less reliable as a support. An illustration of the capsule mounted within a backlit platform hohlraum can be seen in figure 1. The tent material is Formvar (polyvinyl formal,  $C_{31}H_{56}O_{13}$ ) with a density of  $1.23 \text{ g/cm}^3$ . The hydrodynamic perturbation discussed here is seeded around the lift-off ring. In most shots, this ring is circular, at about  $45^\circ$ , and the tent lifts off from the capsule surface at  $10$  to  $15^\circ$  rather than tangentially. In the backlit platform targets, the tent contact along the top and bottom of the capsule is in the shape of an ellipse, with the longer axis along the line of the detector/windows. This is due to the windows in those directions, which prohibit the tent contacting the hohlraum wall at those positions, pulling the lift off point closer to the equator.

To study the case of a non-tent mounted capsule, one shot was performed with the capsule mounted using a thick fill tube. The fill tube, see figure 1, is used to fill the capsule with gas. Nominally, the fill tube has an outer diameter of  $10 \mu\text{m}$  and is inserted into the capsule with a depth of  $30 \mu\text{m}$ . For the tube-mounted capsule the diameter was increased to  $30 \mu\text{m}$  and the insertion depth to  $100 \mu\text{m}$ . This thick tube is called a stalk below. The position of the fill tube with respect to the detector's line of sight can be seen in figure 1 and is about  $50^\circ$  from the radiography axis.

### III. DATA AND SIMULATIONS

Deviations from sphericity of the implosion in-flight seen in the backlit platform described above, is typically described by the Legendre modes. To be more quantitative, the backlit frame is divided into angular sectors, and the radial lineout for each sector is analyzed for the minimum transmission. This radius corresponds approximately to the peak density of the shell. The contours constructed from this radius of all angular sectors is analyzed into a Legendre polynomial series. By repeating the process for all frames the time evolution of the low mode shape,  $P_0$  to  $P_8$ , and implosion velocity are obtained for the in-flight shell during the diagnosed phase [5]. Another metric for the quality of the implosion is the shape

of the x-ray self emission of the hot spot. The hot spot is formed when the fuel is heated and compressed to a high average density. A good correspondence exists between the hot spot perimeter and the 17% contour of the x-ray emission [14].

#### A. Surrogacy between THD and symcap

Targets containing solid DT or tritium-hydrogen-deuterium (THD) fuel layers are more involved to field and prepare, and are intended to have high neutron yields. Gas-filled targets called symcaps are used to study implosion dynamics during the acceleration and peak velocity phase [13]. As it is the total mass of the capsule that dominates the implosion dynamics, in the symcap surrogate, the DT or THD ice fuel layer is replaced by an equivalent mass of plastic. The changes in the target lead to a lower overall convergence of the symcap compared to the layered targets. To test the surrogacy between the two platforms, we have measured the in-flight shape of both symcaps and a backlit layered target. The evolution of  $P_4$ , in absolute units of  $\mu\text{m}$ , for a symcap and a THD target driven with nominally identical conditions are shown in figure 2. This shows comparable in-flight shapes at overlapping times, which allows us to use the easier-to-field symcap platform for shape tuning, rather than the more complex layered capsules. The similar evolution between THD and symcap is also observed for the other  $P$  modes ( $P_0$  to  $P_8$ ). The time integrated self-emission images show a hot spot size for the THD that is about half that of the symcap, however the time integrated  $P_4/P_0$  measurements for the THD and symcap shots are comparable within the error bars.

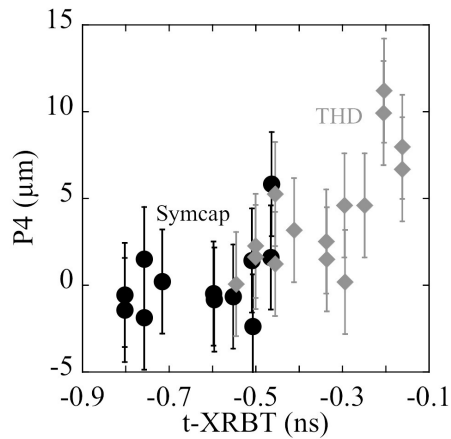


FIG. 2:  $P_4$  evolution of the shell comparison between THD and symcap shows comparable in-flight shapes, illustrating the surrogacy of the easier-to-field symcap platform for tuning. For  $+700 \mu\text{m}$  hohlraum length.

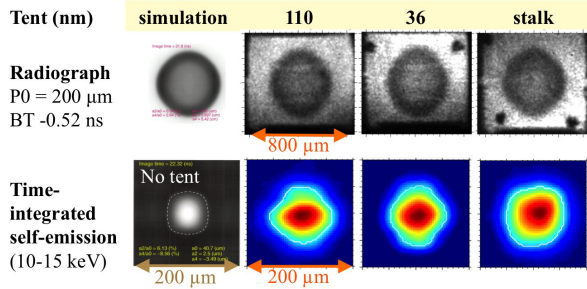


FIG. 3: (Color) In-flight shape and hot spot emission comparison between different tent thickness shots, a stalk shot and a tent-less and stalk-less simulation for nominal hohlraum length.

### B. Influence of the tent on measured $P_4$

Detailed integrated hohlraum-capsule simulations using HYDRA [15], that do not include the tent mounting, show the presence of an in-flight diamond-like (positive)  $P_4$  that phase inverts to square-like (negative)  $P_4$  hotspot self-emission image. The simulated images can be seen in the first column of figure 3 and figure 4 shows the resulting  $P_4$  amplitudes (gray symbols). The swing rate is in agreement with the one observed in [5], and is likely due to early drive asymmetries which lead to residual kinetic energy in the implosion [4, 16].

The black symbols in figure 4 show a summary of the measured  $P_4/P_0$ s for the different tent thicknesses, the radiographs and self emission images for which are shown in figure 3. The in-flight shell is represented by the squares, and the hot spot emission by the circles. Although the tent feature is obvious in the in-flight ra-

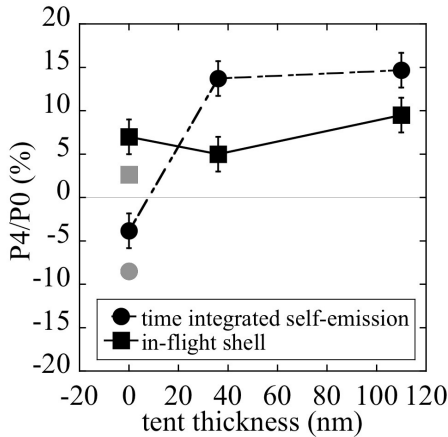


FIG. 4: In-flight shape (squares) and hot spot emission (circles) comparison for the nominal hohlraum length. Simulation data not including a mounting membrane is shown in gray. The experimental data, for shots with different tent thickness and the stalk shot, are shown in black.

diographs, in the form of a pair of horizontal bands, it does not affect the in-flight  $P_4$  as much as it affects the hot spot  $P_4$ . The hot-spot  $P_4$  from self emission is sensitive to the tent as it significantly decreases for the stalk-mounted target. Furthermore, for the stalk shot we observe a swing from a positive in-flight  $P_4$  to negative  $P_4$  in the self emission, which is in agreement with simulations that do not include the tent or the stalk (gray symbols). Even though the simulations do not perfectly capture the shape, i.e. the experimentally observed seems to be more positive, the offset in  $P_4/P_0$  between the time integrated self emission and the in-flight shape match.

### C. Controlling $P_4$ using the hohlraum length

By changing the laser pointing and hohlraum length, the amplitude of the  $P_4$  mode of the in-flight shell can be reduced by moving the location of the outer cones further away from the equator of the hohlraum. To prevent clipping of the outer cones by the laser entrance hole the hohlraum is lengthened by the same amount as the outer beams move. Tent-less HYDRA simulations show that a hohlraum that is 700 μm longer than the nominal length should minimize the in-flight  $P_4$ . This can be seen in figure 5, red symbols.

A series of experiments with different length hohlraums has been performed with a nominal tent thickness of

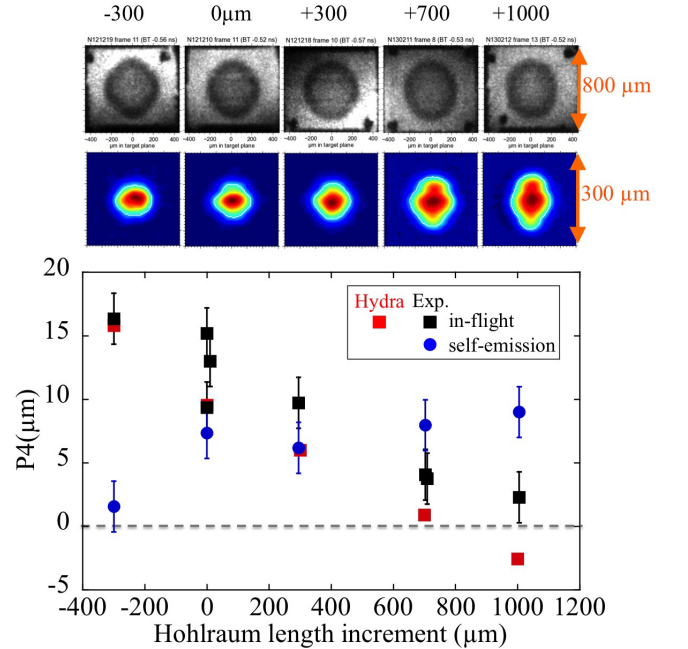


FIG. 5: (Color) The measured  $P_4$  (μm) for in-flight shell at 220 μm (top row, and black squares) match well with the ones from simulations for the length scan (red squares). However, the experimental self-emission images (second row and blue data points) do not match the tent less simulations, which usually show a negative hot spot  $P_4$ .

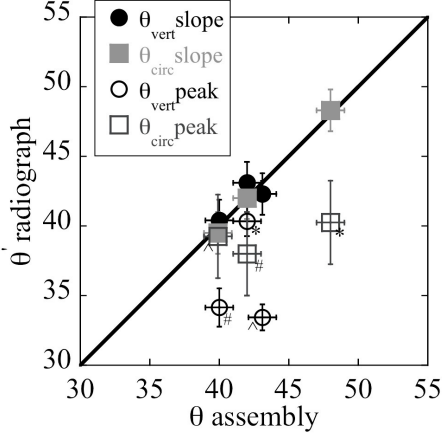


FIG. 6: Latitude of the tent feature extracted from radiography data ( $\theta_{\text{radiograph}}$ ) plotted as a function of the contact position between tent and capsule in the pre-shot target metrology ( $\theta_{\text{assembly}}$ ). The angles from the equator were measured for two directions. For circles, the x-axis is the lift-off position in a vertical plane coming towards the measurement direction (vertical dashed line in figure 7(a),  $\theta_{\text{vert}}$ ). Squares are in the orthogonal plane (circular line out in figure 7(a),  $\theta_{\text{circ}}$ ). For the solid symbols, the vertical axis is one measure of the position of the tent feature in the radiographs, taken as the location half-way up the slope of the tent feature, away from the equator. This location is converted into the angle from the equator of the capsule. These positions are marked with crosses in figures 8(a) and (b). For the open symbols, the vertical axis is the position of the local maximum in transmitted intensity, again converted to angle from the equator. The measurements corresponding to the solid symbols match the lift off position of the tent as measured from the assembly images (x-axis). On the other hand, the position of the peak transmission of the tent features (open symbols) are shifted away from the lift-off latitude. For the open symbols measurements from a single target are indicated by the same subscript symbols.

45 nm. Typical frames of the backlit images, when the implosion capsule is at a radius of  $\approx 220 \mu\text{m}$ , are shown in Figure 5 (top row). The measured in-flight  $P_4$ s for the different hohlraum lengths are also plotted in figure 5, black squares. Both simulations and experimental data show a substantial reduction of the in-flight  $P_4$  with hohlraum length, see also [5]. Figure 5 shows that the diamond shape in-flight  $P_4$  can be reduced for longer hohlraum targets, but that the hotspot emission has a more pronounced and persistent  $P_4$ . This is in contradiction to the simulations, which do not have tents, and is consistent with the notion that the capsule-support tent is significantly affecting the hot-spot images, although, as discussed previously, it has a negligible effect on the in-flight shape analysis.

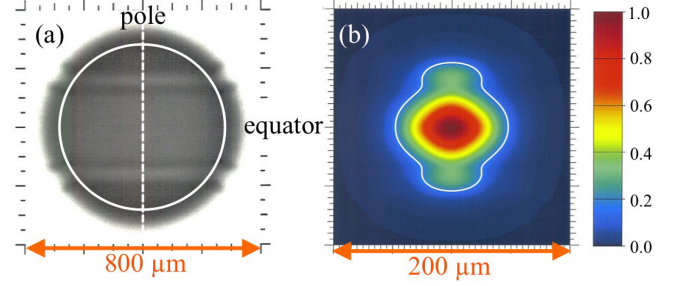


FIG. 7: (Color) Simulated backlit (a) and core emission (b) images showing a feature that approximates the effect of a 45 nm tent. The tent feature is modeled with a groove that is initially  $350 \mu\text{m}$  wide and  $300 \text{ nm}$  deep and initially centered at  $31^\circ$  for (a) and  $40^\circ$  for (b). (a) Image is shown at a time when the outer radius is  $300 \mu\text{m}$ , compare to figure 3. Line outs used in figure 8 are indicated in the simulated image (a). (Shot number N131010)

#### D. Position of the tent features

Though the tent feature in the in-flight shell images does not affect the interpretation of the in-flight shape, it has been shown [17] that it has a significant impact on the areal density and its asymmetries. Clear perturbations, in direct correspondence with the tent features visible in the radiographs, can be seen in the reconstructed mass density maps [17]. For some of the targets, the position where the tents lift off the capsule were measured after target assembly. It should be noted that the latitude at which the tent comes in contact with the shell is not necessarily constant around the target, and that the tent lift-off latitude can therefore vary along the contact ring. For reference, the poles of the capsule lie along the symmetry axis of the cylindrical hohlraum.

Figure 6 shows the latitude of the tent feature in the radiography data as a function of the contact position between tent and capsule in the pre-shot target metrology. Data is shown for three shots, indicated with subscript symbols on the data in the figure. Angles from the radiography data are obtained at two different positions [see figure 7(a)]: The circles labeled as  $\theta_{\text{vert}}$  correspond to a measurement along a vertical line out through the center of the radiography image, as indicated by the dashed white line in figure 7(a). The squares labeled as  $\theta_{\text{circ}}$  correspond to measurements from the circular line out of the image, as indicated by the solid white line in figure 7(a). Examples for the vertical and circular line outs can be seen in figure 8. From these line outs, one can find the position of peak brightness (maximum transmission) of the tent feature, indicated with open symbols in figure 6. Similarly, the position of the maximum slope in the x-ray transmission of the tent feature measured on the side towards the target poles is indicated by solid symbols. (The slope features are marked in the line outs shown below in figure 8.) Figure 6 shows that the position of the slope closely matches the initial tent lift-off position,



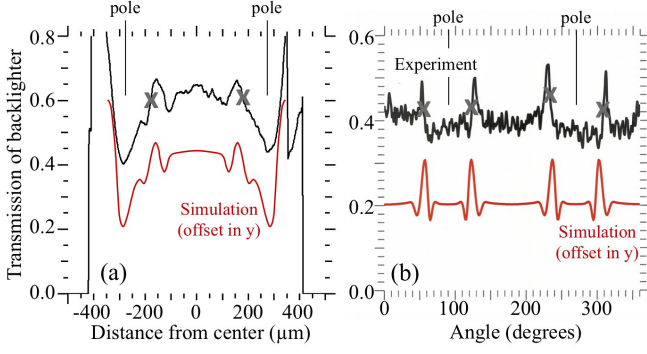


FIG. 8: Comparison of experimentally observed feature from a 45 nm tent with the feature caused by a groove that is 350  $\mu\text{m}$  wide and 300 nm deep, at a time when the outer radius is 300  $\mu\text{m}$ . The simulated line outs are displaced by  $-0.2$  to allow comparison. (a) Vertical line out is averaged over 100  $\mu\text{m}$  laterally. The initial perturbation was centered at  $31^\circ$  from the waist, which positions it properly for this face-centered line out. (b) The circular line out is averaged over 16 microns. The simulated feature on the limb, in (b), is about  $10^\circ$  too close to the waist to match the observed position. ((a) Shot number N131010 and N130314; (b) shot number N131010)

obtained from the pre-shot characterization data, – filled symbols are on the line – while the position of maximum transmission (peak) tends to be  $2\text{--}10^\circ$  closer to the equator than the tent lift-off position. This offset can be expected for a mechanism where the exploding tent seeds a perturbation on the equator-side of the contact ring.

### E. Groove “mock tent” simulations

Early estimates of the tent perturbation were based on simulations using a simplified model of the tent [18], and predicted a tent perturbation less than half as big as is inferred from the observations discussed above. Hammel and coworkers [19, 20] are finding that very high-resolution simulations of the actual tent geometry are in good agreement with the observations described here. Detailed discussion of these simulations is beyond the scope of this paper. In order to form preliminary estimates of the impact of the observed tent feature, it is useful to have an approximate model that could be calibrated to the experimental results, and can be used in simulations to estimate the impact of this larger than expected tent perturbation. The feature as seen in figures 3 and 5 has width of about 70  $\mu\text{m}$ , when the ablation front is at 220  $\mu\text{m}$ ; scaled up to the initial radius of 1130  $\mu\text{m}$ , the initial width would be about 350  $\mu\text{m}$ . Simulations were done with an initially 350  $\mu\text{m}$  wide groove, with the shape of a single sinusoidal wave (wavelength 350  $\mu\text{m}$ ), of various initial groove depths. A groove depth of about 300 nm produces a perturbation that is in reasonable agreement with the observed 110 nm tent perturbation, as shown in figures 7 and 8. The position of the groove

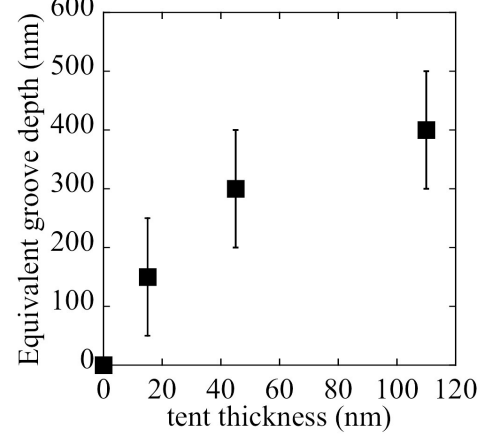


FIG. 9: Depth of 350  $\mu\text{m}$  wide groove that best matches the observed tent perturbation, as a function of tent thickness. Error bars indicate an estimated uncertainty in the equivalence.

that best matches the observed feature is typically about  $10^\circ$  closer to the waist, so that the upper edge of the perturbation is close to the tent lift-off position. The groove depth that best matches the tent perturbation varies non-linearly with the thickness of the tent, as shown in figure 9. This groove is somewhat bigger than has been discussed previously [21], as improved processing of the backlit images has indicated deeper features [22] than were originally estimated.

In these simulations, the shape of the core emission is significantly affected by the tent feature. Figure 7(b) shows a simulated time integrated emission image from a simulation with the same groove depth and width as used for figures 7(a) and 8, located at  $40^\circ$  from the waist. The simulated self emission image is qualitatively similar to the images shown above in figures 3 and 5, with a 9.6  $\mu\text{m}$   $P_4$  Legendre amplitude on the 17% contour. The amplitudes of  $P_4$ , and of the other modes  $P_2$  and  $P_6$ , depend on the angle at which the groove is placed initially, and this location approximately maximizes  $P_4$ .

### F. Influence of the tent thickness on $Y_n$

Possible influence of the tent can also be seen in the decrease of the neutron yield. Figure 10 (triangles) shows measurements of the DD neutron yield plotted against the tent thickness. A yield degradation due to the tent thickness is already seen for this low convergence radiography platform, and is expected to be even more pronounced for higher convergence platforms, closer to the ignition design. Indeed, for the equivalent of a 45 nm tent, the mock tent simulations show a reduction in yield from 40 to 60 % when going from the low to the high convergence platform, see figures 10(circles) and 11. The experimentally observed reduced yield for the 0 nm tent,

see figure 10, which was using a thicker stalk to mount the capsule, is most likely due to the perturbation from the stalk mount.

Simulations initialized with the groove “mock tent” perturbation, described above also show that the tent perturbation has a significant effect on the simulated performance. Figure 10 shows the simulated yield of a typical symcap as the depth of the groove is increased, and figure 11 a layered DT capsule, showing 15-60% yield decrement due to the tent. The impact is not dependent on the width of the groove, as shown in figure 11. The dependence on tent thickness is nonlinear, and the impact is significant for even the thinnest tents.

### G. Rayleigh-Taylor Instability seed and mitigation

Because the mounting membranes are very thin, it was originally estimated that the tent would have acceptable impact on the implosion [18]. However, the data suggests that the tents seed RTIs at the capsule surface from the beginning, which grow throughout the implosion until they eventually (nearly) perforate the capsule, as has been seen in detailed simulations [20] and is suggested by the processed radiography images, see for example figure 10 in [22]. The interpretation of RTI, seeded by the tent contacts, being responsible for the features, is also supported by data taken with a higher adiabat laser pulse shape. These experiments show no visible tent feature in either radiographs or self emission images [23].

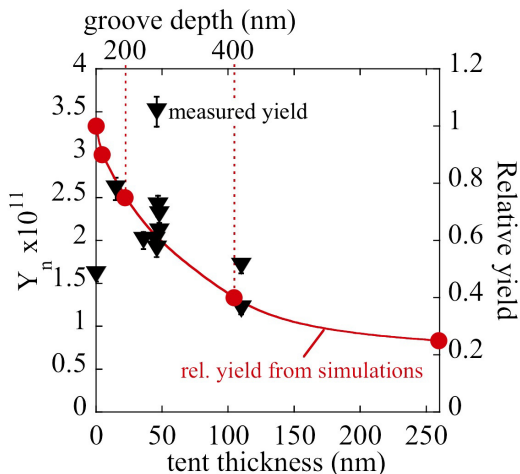


FIG. 10: Measured DD yield from symcap implosions (triangles) vs. tent thickness shows a decrease of the neutron yield for increasing tent thickness. The reduced yield for the 0 nm tent is attributed to the invasive stalk mounting technique for this target. The yield reduction in simulations of a typical symcap implosion is plotted on the right y-axis. In the simulations the capsule was perturbed by a  $350 \mu\text{m}$  wide groove at the location of the tent contact ring with different depths. The groove depth to tent thickness conversion was obtained from figure 9.

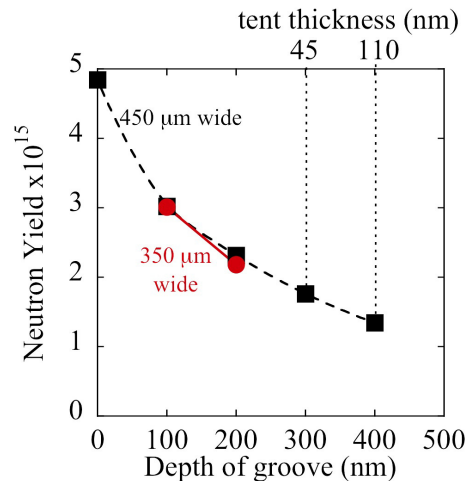


FIG. 11: Yield reduction of a typical low-foot (low adiabat) layered cryogenic (high convergence) implosion (N120321), perturbed by a groove at the location of the tent contact ring.

Simulated high adiabat implosions seeded with a similar groove do not show any visible feature in a radiograph image. The tent feature is not predicted to have a significant effect on the performance of these high adiabat implosions, consistent with their reduced hydrodynamic instability [23–26].

## IV. SUMMARY/CONCLUSIONS

The effect of the tent thickness has been seen in the measured DD yield and the shape of the hot spot self emission. Furthermore the position of the tent features in the radiographs match the tent lift-off positions. These measurements support the interpretation that the tent seeds a perturbation at its lift off positions that leads to a Rayleigh-Taylor instability, which is absent for the stalk case. Due to the reduction of the hydrodynamic instability the impact of the tent is significantly reduced in higher adiabat implosions.

Simulations using an approximate tent model that was calibrated to the experimental results agree with the observed yield degradation caused by the tent. As expected, they predict a significant reduction in yield moving from a low (15-25) to a high (>25) convergence platform.

The influence of the tent feature on the hot spot emission could explain prior inconsistencies between the in-flight (radiograph)  $P_4$  and the core (hot spot emission)  $P_4$ , leading to a reevaluation of the optimum hohlraum length.

This work shows that it is important to use mounting membranes that are as thin as possible, find mitigation strategies, for example in the form of the laser pulse shapes for less instability growth, or alternative mounting strategies, and to keep this tent effect in mind when interpreting results of self-emission shape measurements.



## V. ACKNOWLEDGEMENTS

This work performed under the auspices of the U. S. Department of Energy by Lawrence Livermore National

Laboratory under Contract No. DE-AC52-07NA27344. LLNL-JRNL-664740

- 
- [1] G. H. Miller, E. I. Moses and C. R. Wuest, Nucl. Fusion 44, S228 (2004).
  - [2] J. Lindl, Phys. Plasmas 2, 3933 (1995).
  - [3] S. Atzeni and J. Meyer-ter-Vehn, *The Physics of Inertial Fusion* (Oxford University Press, Oxford, UK, 2007).
  - [4] A. L. Kritcher, R. Town, D. Bradley, D. Clark, B. Spears, O. Jones, S. Haan, P. T. Springer, J. Lindl, R. H. H. Scott, D. Callahan, M. J. Edwards and O. L. Landen Phys. Plasmas 21, 042708 (2014)
  - [5] J. R. Rygg, O. S. Jones, J. E. Field, M. A. Barrios, L. R. Benedetti, G. W. Collins, D. C. Eder, M. J. Edwards, J. L. Kline, J. J. Kroll, O. L. Landen, T. Ma, A. E. Pak, L. Peterson, K. Raman, R. P. J. Town, and D. K. Bradley, Phys. Rev. Lett. 112, 195001 (2014).
  - [6] S. H. Glenzer, B. J. MacGowan, P. Michel, N. B. Meezan, L. J. Suter, S. N. Dixit, J. L. Kline, G. A. Kyrala, D. K. Bradley, D. A. Callahan, E. L. Dewald, L. Divol, E. Dzenitis, M. J. Edwards, A. V. Hamza, C. A. Haynam, D. E. Hinkel, D. H. Kalantar, J. D. Kilkenny, O. L. Landen, J. D. Lindl, S. LePape, J. D. Moody, A. Nikroo, T. Parham, M. B. Schneider, R. P. J. Town, P. Wegner, K. Widmann, P. Whitman, B. K. F. Young, B. Van Wenterghem, L. J. Atherton, E. I. Moses, Science 327, 1228 (2010).
  - [7] Lord Rayleigh, Proceedings of the London Mathematical Society 14: 170177 (1882).
  - [8] G. I. Taylor, Proceedings of the Royal Society of London. Series A, Mathematical and Physical Sciences 201, 1065: 192-196 (1950).
  - [9] J. D. Kilkenny et al, Phys. Plasmas 1, 1379 (1994)
  - [10] S. W. Haan, J. D. Lindl, D. A. Callahan, D. S. Clark, J. D. Salmonson, B. A. Hammel, L. J. Atherton, R. C. Cook, M. J. Edwards, S. Glenzer, A. V. Hamza, S. P. Hatchett, M. C. Herrmann, D. E. Hinkel, D. D. Ho, H. Huang, O. S. Jones, J. Kline, G. Kyrala, O. L. Landen, B. J. MacGowan, M. M. Marinak, D. D. Meyerhofer, J. L. Milovich, K. A. Moreno, E. I. Moses, D. H. Munro, A. Nikroo, R. E. Olson, K. Peterson, S. M. Pollaine, J. E. Ralph, H. F. Robey, B. K. Spears, P. T. Springer, L. J. Suter, C. A. Thomas, R. P. Town, R. Vesey, S. V. Weber, H. L. Wilkens, and D. C. Wilson, Phys. Plasmas 18, 051001 (2011).
  - [11] D. A. Callahan, N. B. Meezan, S. H. Glenzer, A. J. MacKinnon, L. R. Benedetti, D. K. Bradley, J. R. Celeste, P. M. Celliers, S. N. Dixit, T. Döppner, E. G. Dzenitis, S. Glenn, S. W. Haan, C. A. Haynam, D. G. Hicks, D. E. Hinkel, O. S. Jones, O. L. Landen, R. A. London, A. G. MacPhee, P. A. Michel, J. D. Moody, J. E. Ralph, H. F. Robey, M. D. Rosen, M. B. Schneider, D. J. Strozzi, L. J. Suter, R. P. J. Town, K. Widmann, E. A. Williams, M. J. Edwards, B. J. MacGowan, J. D. Lindl, L. J. Atherton, G. A. Kyrala, J. L. Kline, R. E. Olson, D. Edgell, S. P. Regan, A. Nikroo, H. Wilkins, J. D. Kilkenny, A. S. Moore, Phys. Plasmas 19, 056305 (2012).
  - [12] D.G. Hicks et al., Phys. Plasmas 17, 102703 (2010).
  - [13] D.G. Hicks et al., Phys. Plasmas 19, 122702 (2012).
  - [14] G. A. Kyrala, J. Kline, S. Dixit, S. Glenzer, D. Kalantar, D. Bradley, N. Izumi, N. Meezan, O. Landen, D. Callahan, S. V. Weber, J. P. Holder, S. Glenn, M. J. Edwards, J. Koch, L. J. Suter, S. Haan, R. P. J. Town, P. Michel, O. Jones, S. Langer, J. D. Moody, E. L. Dewald, T. Ma, J. Ralph, A. Hamza, E. Dzenitis, and J. Kilkenny, Phys. Plasmas 18, 056307 (2011).
  - [15] M. M. Marinak, S. W. Haan, T. R. Dittrich, R. E. Tipton and G. B. Zimmerman, Phys. Plasmas 5, 1125 (1998).
  - [16] R.P.J. Town et al, Phys. Plasmas 21, 056313 (2014).
  - [17] R. Tommasini (in preparation)
  - [18] S. W. Haan, J. D. Lindl, D. A. Callahan, D. S. Clark, J. D. Salmonson, B. A. Hammel, L. J. Atherton, R. C. Cook, M. J. Edwards, S. Glenzer, A. V. Hamza, S. P. Hatchett, M. C. Herrmann, D. E. Hinkel, D. D. Ho, H. Huang, O. S. Jones, J. Kline, G. Kyrala, O. L. Landen, B. J. MacGowan, M. M. Marinak, D. D. Meyerhofer, J. L. Milovich, K. A. Moreno, E. I. Moses, D. H. Munro, A. Nikroo, R. E. Olson, K. Peterson, S. M. Pollaine, J. E. Ralph, H. F. Robey, B. K. Spears, P. T. Springer, L. J. Suter, C. A. Thomas, R. P. Town, R. Vesey, S. V. Weber, H. L. Wilkens, and D. C. Wilson, Phys. Plasmas 18, 051001 (2011).
  - [19] B. A. Hammel, Bulletin of APS DPP 2014
  - [20] B. A. Hammel, (in preparation)
  - [21] S.W. Haan, Bulletin of APS DPP 2013
  - [22] J. E. Field, J. R. Rygg, M. A. Barrios, L. R. Benedetti, T. Döppner, N. Izumi, O. Jones, S. F. Khan, T. Ma, S. R. Nagel, A. Pak, R. Tommasini, D. K. Bradley and R. P. J. Town, Review of Scientific Instruments 85, 11E503 (2014).
  - [23] O. A. Hurricane, D. A. Callahan, D. T. Casey, E. L. Dewald, T. R. Dittrich, T. Döppner, M. A. Barrios Garcia, D. E. Hinkel, L. F. Berzak Hopkins, P. Kervin, J. L. Kline, S. Le Pape, T. Ma, A. G. MacPhee, J. L. Milovich, J. Moody, A. E. Pak, P. K. Patel, H.-S. Park, B. A. Remington, H. F. Robey, J. D. Salmonson, P. T. Springer, R. Tommasini, L. R. Benedetti, J. A. Caggiano, P. Celliers, C. Cerjan, R. Dylla-Spears, D. Edgell, M. J. Edwards, D. Fittinghoff, G. P. Grim, N. Guler, N. Izumi, J. A. Frenje, M. Gatu Johnson, S. Haan, R. Hatarik, H. Herrmann, S. Khan, J. Knauer, B. J. Koziolowski, A. L. Kritcher, G. Kyrala, S. A. Maclaren, F. E. Merrill, P. Michel, J. Ralph, J. S. Ross, J. R. Rygg, M. B. Schneider, B. K. Spears, K. Widmann, and C. B. Yeamans, Physics of Plasmas 21, 056314 (2014); doi: 10.1063/1.4874330
  - [24] T. R. Dittrich, O. A. Hurricane, D. A. Callahan, E. L. Dewald, T. Döppner, D. E. Hinkel, L. F. Berzak Hopkins, S. LePape, T. Ma, J. Milovich, J. C. Moreno, P. K. Patel, H.-S. Park, B. A. Remington, and J. Salmonson, Phys. Rev. Lett. 112, 055002 (2014).
  - [25] V. A. Smalyuk, D. T. Casey et al., Phys. Rev. Lett. 112, 185003 (2014).

- [26] K. S. Raman, V. A. Smalyuk, D. T. Casey et al., *Physics of Plasmas* 21, 072710 (2014)